Available online at www.sciencedirect.com
ScienceDirect
Trans. Nonferrous Met. Soc. China 34(2024) 435−452
Transactions of Nonferrous Metals Society of China
www.tnmsc.cn

Growth and characterization of plasma electrolytic oxidation coating on 60%SiC_p/2009 aluminum matrix composite

Yi-zhao LIAO[1,2], Xing-ping WANG[1,2], Chuan-li GAO[1,2], Qian ZHOU[1,2], Chi XU[1,2], Xiao-yue JIN[2], Jian-cheng DU[1,2], Wen-bin XUE[1,2], Yong-zhong ZHANG[3]

1. Key Laboratory of Beam Technology of Ministry of Education, College of Nuclear Science and Technology, Beijing Normal University, Beijing 100875, China;
2. Institute of Radiation Technology, Beijing Academy of Science and Technology, Beijing 100875, China;
3. GRINM Group Corporation Limited, Beijing 100088, China

Received 27 August 2022; accepted 17 March 2023

Abstract: A ceramic coating on 60vol.%SiC_P/2009 aluminum matrix composite was prepared by plasma electrolytic oxidation (PEO) in silicate solution. The microstructure, composition and wettability of the PEO coating and its corrosion resistance were investigated. The generation mechanism of spark discharge on the SiC particles surface was also discussed. It is found that the insoluble compound (SiO_2) from silicate solution is vital for the ignition of spark discharge on the SiC particles surface. The defects in the Al−Si−O compounds provide a priority path for the conduction of discharge current on the SiC particles surface. A uniform coating of 5.5 μm was fabricated after 1200 s. Moreover, with the increase of time, the surface free energy of PEO coating reached the maximum of 37.10 mJ/cm^2 at 40 s, and then decreased to 25.95 mJ/cm^2 at 1200 s. Furthermore, the corrosion resistance of the composite was greatly improved by PEO treatment.

Key words: plasma electrolytic oxidation; aluminum matrix composite; SiC reinforcement particles; spark discharge; wettability; corrosion resistance

1 Introduction

Plasma electrolytic oxidation (PEO) has been considered as one of the cost-effective and eco-friendly surface treatment techniques for valve metals (Al, Mg, Ti, etc.) and their alloys [1,2]. The spark discharges occur at the metal/electrolyte interface when the applied voltage exceeds a critical value [3,4]. The features of spark discharges determine the thermal and chemical conditions on the metal surface, and they play a vital role in the structures and phase constituents of PEO coatings [5,6].

In recent years, the PEO technique has also been applied in the surface treatment of the metal matrix composites (MMCs) [7−10]. The reinforcement particles in MMCs include SiC, Al_2O_3 and B_4C, etc. [11]. SiC is one of the most common reinforced phases due to its low cost and excellent performance [12]. However, SiC particles as ceramic phase greatly affect the PEO discharge process and the growth of PEO coatings on metal matrix composites. Therefore, the influence of SiC particles in MMCs on the growth process of PEO coatings has attracted great attention [13−15].

WANG et al [13] reported that SiC particles inhibited the occurrence of spark discharges in the early stage of PEO treatment on (5−15 vol.%) SiC_p/AZ91 Mg matrix composite, and the growth efficiency of the PEO coating decreased with the increase of SiC volume fraction. Moreover, in our

Corresponding author: Wen-bin XUE, Tel: +86-10-62207222, E-mail: xuewb@bnu.edu.cn
DOI: 10.1016/S1003-6326(23)66409-X

previous work [14,15], it was found that most of SiC particles in 15vol.%SiC_P/2024 Al MMC and 6vol.%SiC_P/AZ31 Mg MMC were melted and transformed to silicon oxide at high temperatures in the plasma discharge channels, but a few SiC particles were still remained in the PEO coating. However, these studies were focused on the PEO treatment of MMCs with low volume fraction reinforced phase (<35 vol.%), and the information about the PEO treatment for high volume fraction SiC-reinforced MMCs is very limited [16].

Recently, the MMCs with high volume fraction SiC reinforcement (≥35 vol.%) have attracted considerable attention, because of their potential application in electronic packaging [17,18]. The preparation of insulating films on the surface of the MMCs is conductive to maintain the insulation between the electronic components. Therefore, it is interesting to study whether a continuous and well-bonded insulating coating can be fabricated on the MMCs with high volume fraction SiC reinforcement by PEO technique.

On the other hand, the presence of continuous insulating thin film on the metal surface is a prerequisite for the occurrence of dielectric breakdown and the following spark discharge [1], but it is almost impossible to breakdown the insulating SiC particles in MMCs under several hundred voltages. Therefore, it is meaningful to investigate the generation mechanism of discharge spark and the growth of PEO coating on the surface of SiC particles in MMCs.

In this work, the growth process, morphology, composition, phase constituent, wettability and surface free energy of the PEO coating on 60vol.%SiC_P/2009 aluminum (Al) matrix composite were investigated, and the spark discharge mechanism of SiC reinforcement particles was discussed. Meanwhile, the electrochemical corrosion behavior of bare and PEO-coated composites was evaluated.

2 Experimental

The as-received 60vol.%SiC_P/2009 Al matrix composite prepared by powder metallurgic method was cut into rectangular coupons (25 mm × 15 mm × 5 mm). The nominal composition of 2009 Al alloy was 3.8 wt.% Cu, 1.4 wt.% Mg, 0.05 wt.% Fe, 0.14 wt.% Si, and Al balance. These coupons were polished with SiC abrasive papers, cleaned by an ultrasonic cleaner with ethanol, and dried sequentially. The microstructure of 60vol.%SiC_P/2009 Al MMC was observed by optical microscope (OM, Carl Zeiss Image A2m).

During the PEO treatment, the Al MMC sample and the stainless steel plate were served as anode and cathode, respectively. The PEO process was carried out at different time from 2 to 1200 s under constant voltage mode with the frequency of 150 Hz and the duty cycle of 45% in silicate solution, which consisted of 14 g/L $Na_2SiO_3·9H_2O$ and 1 g/L KOH. The voltage of 440 V was simultaneously applied to the Al MMC anode when the power supply was switched on, meanwhile, the voltage and current were recorded by a data acquisition system.

Optical emission spectroscopy (OES) during PEO treatment on 60vol.%SiC_P/2009 Al matrix composite was collected using an optical emission spectrometer (AvaSpec−2048). The dark background was acquired and subtracted before OES collection experiment. Then, the acquired OES data were analyzed by Plasus Specline 2.1 software. The morphologies and compositions of PEO coatings were observed by scanning electron microscope (SEM, Hitachi S−4800) equipped with energy dispersive spectroscopy (EDS). The surface chemical states of PEO coatings were analyzed by X-ray photoelectron spectroscopy (XPS, VG ESCALABMKII). The C 1s peak from adventitious carbon at 284.8 eV was used to correct the charge shifts. Meanwhile, the phase constituents of the PEO coatings were determined by X-ray diffraction (XRD, X' Pert Pro MPD, Bragg-Brentano geometry, 40 kV and 40 mA) with a Cu K_α radiation (λ= 1.54 Å) and a step size of 0.0330° in the range of 10°−80°. The composition depth profiles of the polished and coated Al MMCs were analyzed by a glow discharge optical emission spectrometer (GDOES, SPECTRUMA GDA750).

The surface roughness of the polished Al MMC and the PEO coatings fabricated at different oxidation time was evaluated by the MMD-CERM3600 roughness profiler. The HARKE-SPCAX1 contact angle tester was utilized to measure the contact angles of water and *n*-hexadecane on the surface of Al MMC and PEO coatings, then the surface free energies of Al MMC and PEO coatings were calculated based on the

results of contact angles. In addition, the corrosion resistances of the bare Al MMC and PEO-coated Al MMC were evaluated using electrochemical impedance spectroscopy (EIS) and potentiodynamic polarization tests in 3.5 wt.% NaCl solution by a PARSTAT 2273 (Princeton Applied Research, USA) workstation with a tri-electrode system at ambient temperature. The bare or PEO-coated Al MMC, Pt coil and saturated calomel electrode (SCE) were used as the working electrode, counter electrode and reference electrode, respectively. Potentiodynamic polarization tests were carried out at a scan rate of 1 mV/s. EIS tests were performed at the open circuit potential with an AC amplitude of 10 mV over the frequency ranging from 1 MHz to 0.01 Hz. EIS plots were fitted using the ZSimpWin software.

3 Results

3.1 Surface morphologies and compositions of 60vol.%SiC_p/2009 Al MMC

The optical micrograph of 60vol.%SiC_p/2009 Al MMC is shown in Fig. 1. It is observed that SiC particles with an average size of about 14 μm uniformly distribute in the Al matrix. The EDS element mappings of 60vol.%SiC_p/Al MMC in Fig. 2 indicate that the localized enrichment of Al and Si elements is obvious in the Al matrix, while the distribution of C element is relatively uniform. Moreover, Fig. 2(a) shows that the surface of polished Al MMC is uneven, the EDS point analysis demonstrates that the convex region in Fig. 2(a) contains 56.63 at.% Si, 43.22 at.% C and 0.15 at.% Al, which is considered to be a SiC particle (see Point *A* in Fig. 2(a)).

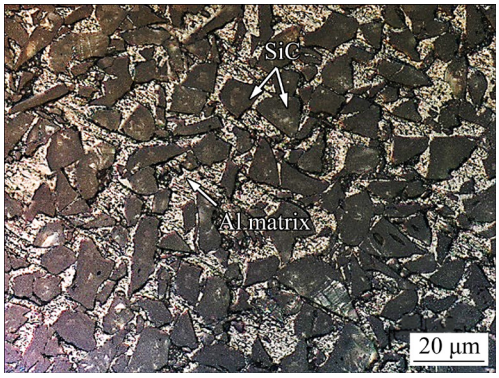

Fig. 1 Metallographic microstructure of 60vol.%SiC_p/Al MMC

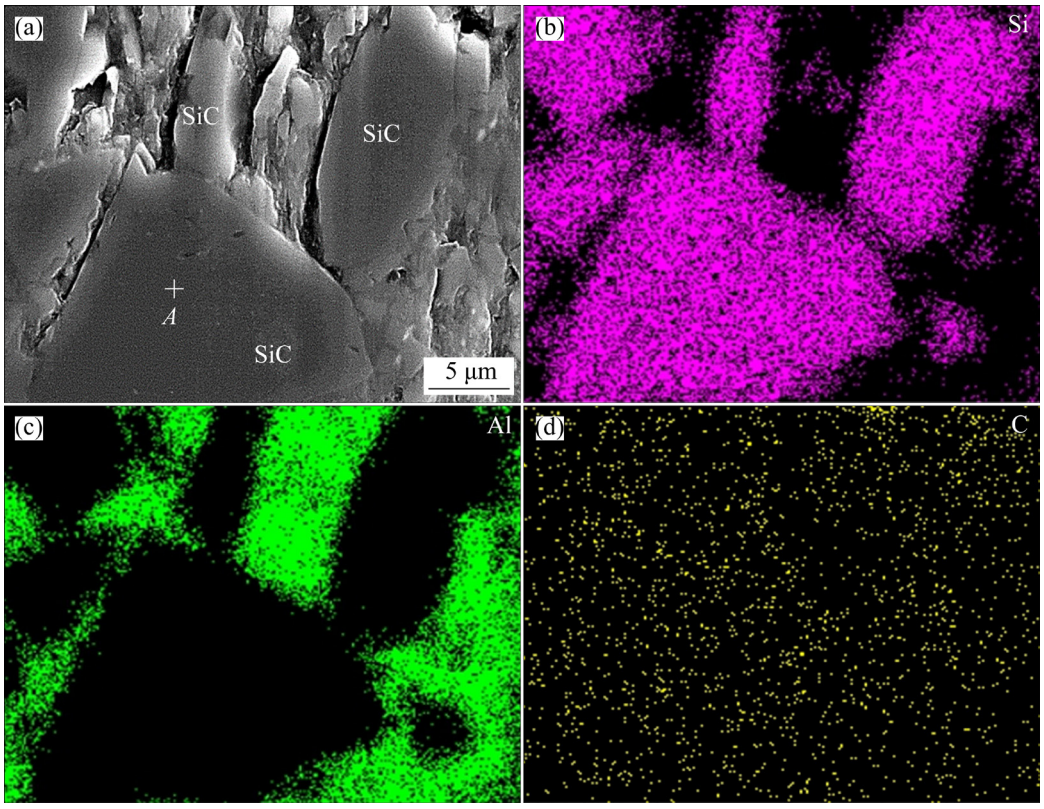

Fig. 2 Surface morphology and elemental mappings (b−d) of 60vol.%SiC_p/Al MMC: (a) SEM image; (b) Si; (c) Al; (d) C

3.2 Electrical characteristics and optical emission spectroscopy

Figure 3 shows the electrical characteristics of the PEO process of the 60vol.%SiC_P/2009 Al MMC in silicate solution. It is observed that the positive voltage rapidly reaches the preset value of 440 V within 1 s, and the current density also reaches the maximum value of 1.41 A/cm^2 in the meantime. Then, the applied voltage keeps at 440 V, while the current density quickly decreases and stabilizes at about 0.22 A/cm^2 after 40 s.

The typical optical emission spectroscopy (OES) spectrum during the PEO process of the 60vol.%SiC_P/2009 Al MMC in silicate solution is revealed in Fig. 4. The symbols I and II represent the neutral atom and singly ionized atom, respectively. The emission of a continuum between 450 and 750 nm in Fig. 4 is caused by the collision-radiative recombination and bremsstrahlung radiation of electrons [19,20]. In Fig. 4, the Al I and Cu I spectral lines are ascribed to the Al matrix,

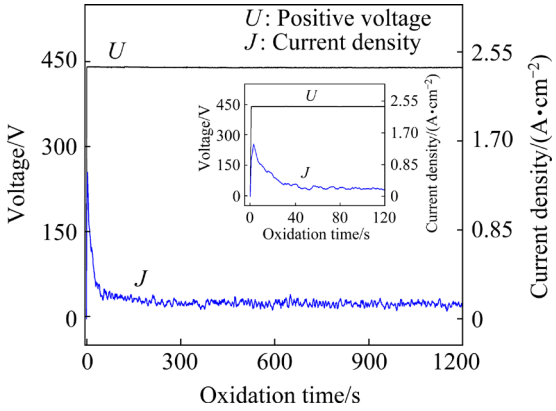

Fig. 3 Dependence of applied voltage and current density on oxidation time during PEO process

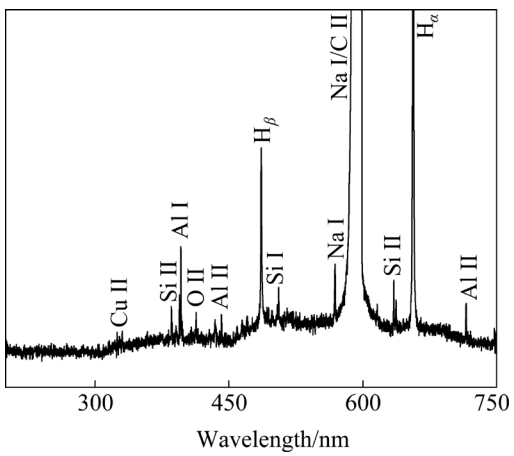

Fig. 4 Optical emission spectrum during PEO process of 60vol.%SiC_P/2009 Al MMC in silicate solution

while Na I, H_α, H_β and O I originate from the silicate solution. The Si spectral lines mainly come from silicate electrolyte entering into discharge channels, but the SiC particles in the 60vol.%SiC_P/2009 Al MMC also participate in the spark discharge process and emit the Si and C spectral lines. However, the C II spectral line at 589.09 nm from SiC particles overlaps with Na I spectral line [21].

Under the partial local thermal equilibrium (PLTE) condition, the electron temperature (T_e) is approximately equal to the temperature of plasma discharge region [20]. Plasma electron concentration (N_e) is used to determine whether the plasma discharge region meets the PLTE condition [19,20]. The minimum N_e to meet PLTE condition is 4.13×10^{21} m^{-3} [19,20]. The Stark broadening of the H_β line is usually utilized to calculate N_e in the plasma discharge region [20]. It is found that the N_e obtained in this experiment is in the range of 1.04×10^{22}–2.22×10^{22} m^{-3}, which is higher than the 4.13×10^{21} m^{-3}. Hence, the PLTE in the plasma discharge region during the PEO treatment on Al MMC has been reached in the present condition, and then the T_e can be calculated on the basis of OES.

According to the theory of atomic emission spectrum, the energy will be released in the form of light radiation to generate atomic emission spectroscopy when the excited atoms transition from a high level to a low level [19]. Under the PLTE condition, when the relative spectral line intensities of the same atomic or ionic species are known, the electron temperature (T_e) can be calculated from Eq. (1) [19,20]:

$$\frac{I_1}{I_2}=\frac{A_1g_1\lambda_2}{A_2g_2\lambda_1}\exp\left(-\frac{E_1-E_2}{kT}\right) \tag{1}$$

where I_1, A_1, g_1, λ_1, E_1 and I_2, A_2, g_2, λ_2, E_2 are relative intensity, transition probability, statistical weight of upper level, wavelength and excitation energy of the two emission spectra line, respectively, moreover, and kT is the thermal energy.

In this work, the plasma electron temperature (T_e) is calculated by the line intensity ratio of H_α at 656.2 nm and H_β at 486.1 nm. As exhibited in Fig. 5, the T_e is 5000−12000 K, which is in accordance with that in PEO process of Al alloy [19,22]. The curve of T_e vs time is similar to the T_e evolution during the PEO process on SiC_P/AZ31 and Al_2O_3−

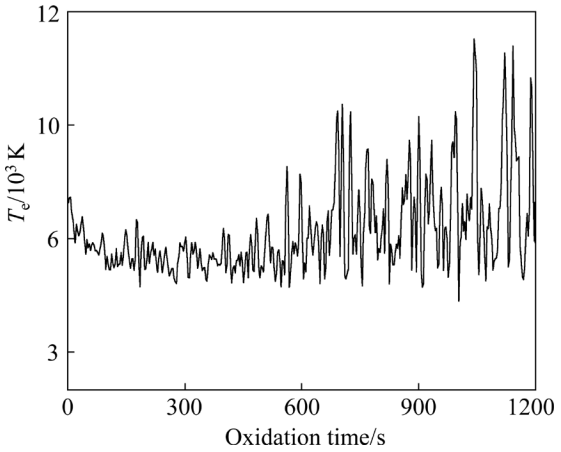

Fig. 5 Dependence of plasma electron temperature on oxidation time in silicate solution

$SiO_{2(sf)}$/AZ91 Mg metal matrix composites [15]. As shown in Fig. 5, the T_e in the initial stage of PEO process is about 7000 K, then it fluctuates around 5500 K after 150 s. Several obvious spike peaks appear after 700 s, which are attributed to the calculation error of T_e rather than the occurrence of big sparks, because the OES signals are weak in the later stage of PEO process [22].

3.3 Surface morphologies and compositions of PEO coatings

Figure 6 displays the surface morphologies of the PEO-treated Al MMC at different oxidation time in the silicate solution. The PEO coating is discontinuous at 2 s and some SiC particles are still visible on the surface of Al MMC as displayed in Fig. 6(a) and its enlarged image (see Fig. 6(b)). Moreover, EDS element mapping in Fig. 7 reveals a non-uniform composition distribution on the surface of Al MMC at 2 s. As shown in Fig. 7(a), the Si element map demonstrates that the area at Point 1 in Fig. 6(b) is a SiC particle. Furthermore, from the center of SiC particle to SiC/Al interface denoted by an arrow in Fig. 6(b), the concentrations of Si and C elements gradually decrease, while the concentrations of Al, O, Na and K elements gradually increase (see Table 1). It implies that spark discharge preferentially occurs on the Al matrix.

Figure 6(b) also shows that the residual discharge micro-pores mainly focus on the Al-rich region and some discharge micro-pores can be also observed near the edge of the SiC particle. It implies that spark discharge also appears at the SiC/Al interface in the initial 2 s. However, the discharge micro-pores are hardly observed in the central region on the surface of the SiC particle, only some micro-cracks can be found on the center of the SiC particle. These micro-cracks might be related to the difference of the thermal expansion coefficients between SiO_2 (0.55×10^{-6} K^{-1}) and SiC (4×10^{-6} K^{-1}) [23].

When the oxidation time reaches 5 s, the number of residual discharge micro-pores near the edge of SiC particles significantly increases. Meanwhile, some fine discharge micro-pores also appear on the center of SiC particles (see Fig. 6(c)), which implies that the spark discharge gradually extends from the SiC/Al interface to the center of SiC particles. Furthermore, the boundary between SiC and Al matrix is indistinguishable, because some compounds accumulate at the SiC/Al interface. EDS analysis confirms that these compounds contain 26.85 at.% Si, 9.26 at.% Al, 57.61 at.% O, 5.27 at.% C, 0.58 at.% Na and 0.43 at.% K, which are considered to be SiO_2 and a little Al−Si−O compounds (see Point 6). Moreover, due to the thermal stress generated from the rapid solidification of molten oxides in the spark discharge channels, more micro-cracks appear on the surface of SiC particles, which accelerates the oxidation of SiC particles.

Table 1 EDS element analysis data of selected points in Fig. 6 (at.%)

Point	Si	Al	O	C	Na	K
1	54.53	0.52	33.12	11.64	0.10	0.09
2	57.37	0.52	37.21	4.59	0.14	0.17
3	49.99	1.45	43.88	4.35	0.16	0.17
4	38.29	17.21	41.06	3.03	0.26	0.15
5	24.58	24.82	46.93	3.51	0.07	0.09
6	26.85	9.26	57.61	5.27	0.58	0.43
7	17.43	11.06	65.85	3.94	1.17	0.55
8	29.78	2.09	57.88	8.79	0.83	0.63
9	26.03	12.54	56.09	4.34	0.57	0.43
10	28.08	2.53	61.91	4.77	2.04	0.67
11	29.9	3.43	61.59	2.28	2.06	0.74
12	27.01	0.08	69.71	2.29	0.61	0.30
13	33.25	13.96	46.21	5.29	0.48	0.81

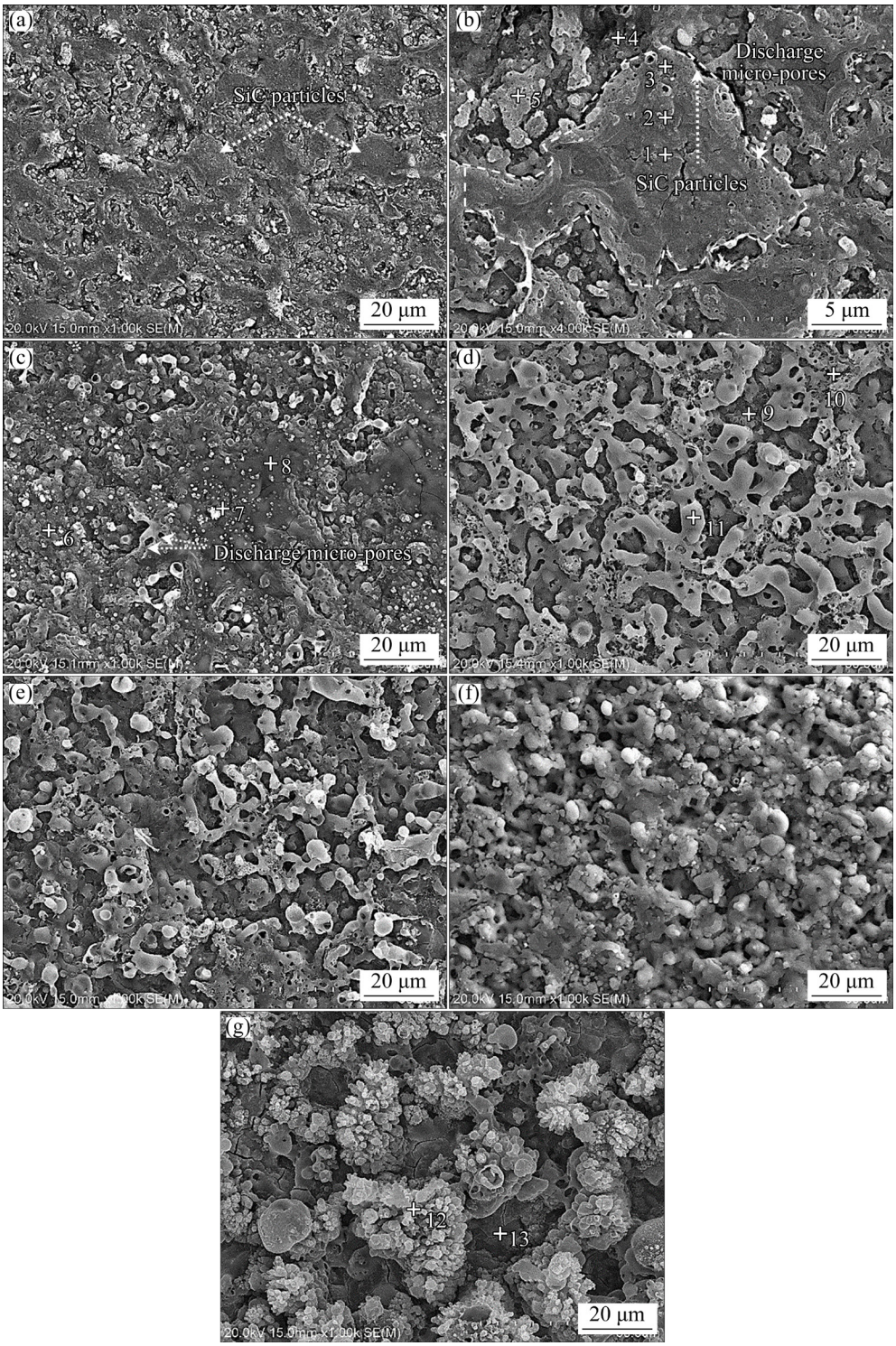

Fig. 6 Surface morphologies of PEO coatings on 60vol.%SiC_p/2009 Al MMC in silicate solution at different oxidation time: (a) 2 s; (b) Enlarged image of (a); (c) 5 s; (d) 20 s; (e) 40 s; (f) 120 s; (g) 1200 s

At the oxidation time of 20 s, many large protrusions cover on the surface of Al MMC, and SiC particles are hardly observed, as shown in Fig. 6(d). EDS analysis of Point 11 confirms that the large protrusions contain 29.9 at.% Si, 3.43 at.% Al, 61.59 at.% O, 2.28 at.% C, 2.06 at.% Na and 0.74 at.% K, which are considered to be Al−Si−O compounds. The melting points of SiC, SiO_2 and Al_2O_3 are 3003, 1999 and 2327 K, respectively [19,24,25], and the ratio of Si_xO_y/Al_zO_t in the PEO coating is high due to the high Si content in the Al MMC, thus the melting temperature of the oxides in

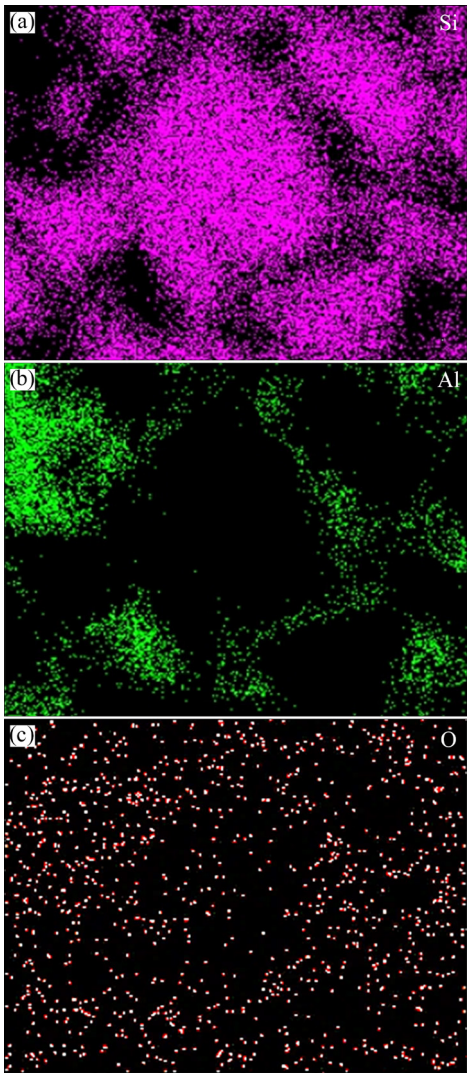

Fig. 7 Elemental mappings of Fig. 6(b): (a) Si; (b) Al; (c) O

the PEO coating declines. As the fluidity of the oxides increases, the surface morphology of the PEO coating is more uniform. Moreover, the oxide coating in the Si-rich region (see Point 10) is looser than that in the Al-rich region (see Point 9). This is similar to the morphology of PEO coatings on Al−Si alloys [26,27].

Many nodules appear on the surface of the Al MMC as displayed in Fig. 6(f) at 120 s, which reveals a typical morphology of PEO coating [1]. At this time, a relative uniform and complete PEO coating is formed on the 60vol.%SiC_P/2009 Al MMC. When the oxidation time reaches 1200 s, as shown in Fig. 6(g), a continuous PEO coating is covered on the surface of the Al MMC. However, the PEO coating in Fig. 6(g) is relatively rough and many grains are aggregated into cauliflower-like oxide areas.

As described in some papers [1,4], the localized oxides will be molten in plasma discharge channels with the high temperature up to 5000 K. When the plasma discharge is quenched, the molten oxides in the channels are solidified rapidly and deposited on the channels, resulting in the coating growth. After 1200 s PEO treatment on Al MMC, many molten oxides are accumulated to form cauliflower-like morphology on the surface of coating due to the repeated spark discharge in these regions. It is in accordance with the surface morphology of PEO coatings as reported by KASEEM et al [1].

3.4 Cross-sectional microstructures and compositions of PEO coatings

Figure 8 shows composition profiles of 60vol.%SiC_p/Al MMC and PEO-coated Al MMC at 5, 120, and 1200 s. As exhibited in Fig. 8(a), an adsorbed layer of 0.08 μm in thickness and a passive layer of 0.07 μm in thickness are formed on the surface of the polished Al MMC sample. The relative intensities of H and O elements in the adsorbed layer are rather high, which implies that some water molecules in the atmosphere are absorbed on the surface of the Al MMC [28,29]. It is also observed that the intensities of H and O elements rapidly decrease in the passive layer due to the formation of passive film in the region of Al matrix as shown in Fig. 8(a). The strong Si and C peaks at 0.11 μm in depth of the passive layer indicate that the bulk SiC particles on the surface of the Al MMC might not be covered by passive film. Moreover, because the hardness of SiC particles is much higher than that of Al matrix, the surface of Al MMC is uneven and SiC particles protrude after polishing, resulting in the Al peak behind C and Si peaks as revealed in Fig. 8(a).

The composition profiles of coated Al MMC at different oxidation time are displayed in Figs. 8(b−d). On the surface of PEO coating, the enrichment of Si element is related to the deposited silicate electrolyte, and the enrichment of O and H elements is ascribed to the absorbed water molecules in the atmosphere. Moreover, the C element comes from the absorbed carbon particles or CO_2 in the atmosphere [21,28,29]. In Fig. 8(b), the Si and C peaks are strong at 0.26 μm in depth of the PEO coating, which implies that a uniform PEO

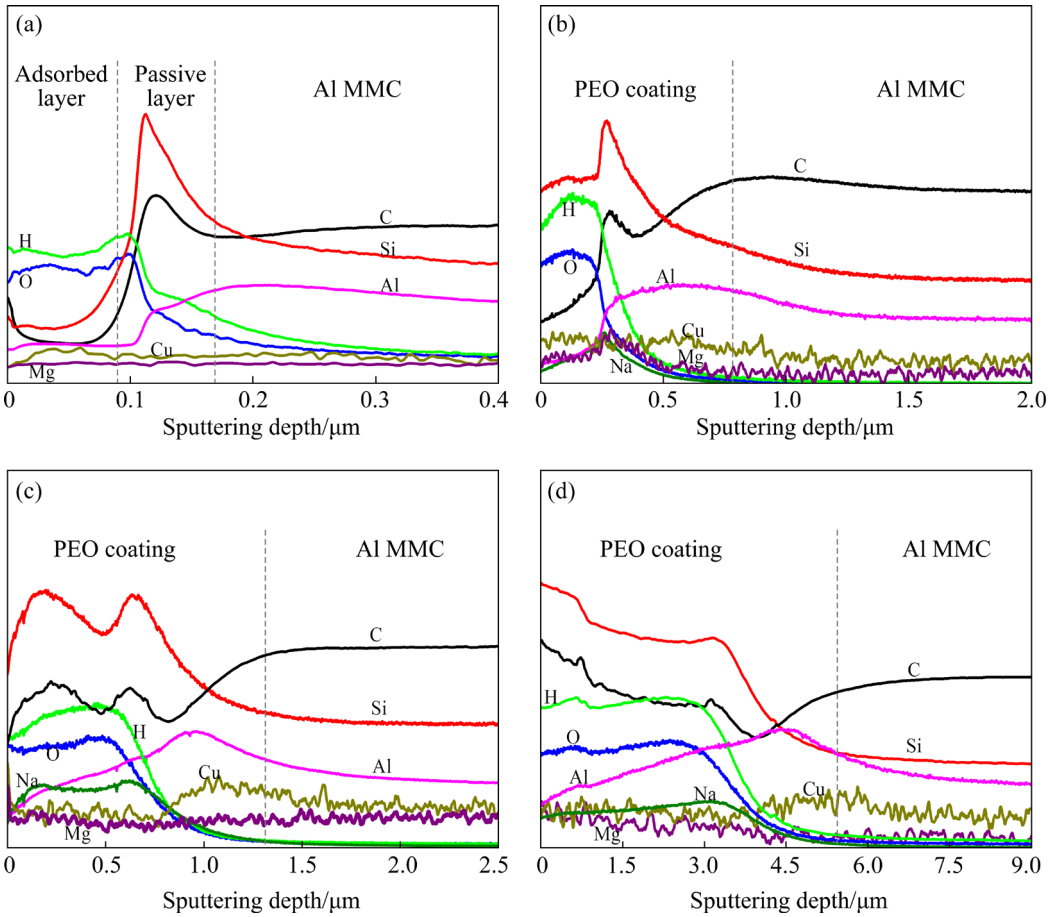

Fig. 8 GDOES composition depth profiles of PEO-treated Al MMC at different oxidation time in silicate solution: (a) Polished 60vol.%SiC_p/2009 Al MMC; (b) 5 s; (c) 120 s; (d) 1200 s

coating has not been formed on the surface of Al MMC at 5 s. It is consistent with the surface morphology in Fig. 6(c). The relative intensities of Al and Cu elements in the PEO coating increase with the increase of oxidation time, meanwhile, an Al peak appears at 0.95 μm in depth (see Fig. 8(c)). It suggests that more Al matrix participates in the PEO process. On the other hand, Fig. 9(a) indicates that the thickness of PEO coating is up to 5.5 μm at 1200 s, which leads to the further reduction of the intensities of Si and C peaks in Fig. 8(d). Furthermore, Fig. 9(a) shows that no visible cracks are observed at the interface between the Al MMC and PEO coating. EDS mappings of Si, Al, C and O elements of cross-sectional sample are displayed in Figs. 9(b−e), respectively. It is found that the distribution of Si element is not uniform, and the Si content in some regions of the PEO coating is high, which indicates that there are some residual SiC particles in the coating. It is consistent with the result of the appearance of Si and C peaks in the PEO coating in Fig. 8(d).

3.5 Phase constituents of PEO coatings

Figure 10 exhibits the phase constituents of PEO-coated Al MMC at different oxidation time in silicate solution. The PEO coatings at 120 and 1200 s are composed of γ-Al_2O_3 and mullite ($3Al_2O_3{\cdot}2SiO_2$) phases. The Al and SiC peaks come from the Al matrix. The intensities of Al and SiC peaks of the coated-Al MMC at 1200 s are much lower than that at 120 s, while the intensity of γ-Al_2O_3 in the PEO coating at 1200 s is higher than that at 120 s. This implies that more Al matrix involves in the plasma discharge process and the thickness of the PEO coating increases with increasing the oxidation time. Moreover, a wide amorphous diffraction peak at 15°−30° for coated Al MMC at 1200 s is detected, which is attributed to the amorphous SiO_2 phase in the PEO coating [30]. During the PEO treatment, the molten aluminum is quickly oxidized to form γ-Al_2O_3 phase under a high cooling rate up to 10^8 K/s [31,32]. However, α-Al_2O_3 phase is not detected in the PEO coating (see Fig. 10), because its nucleation rate is lower

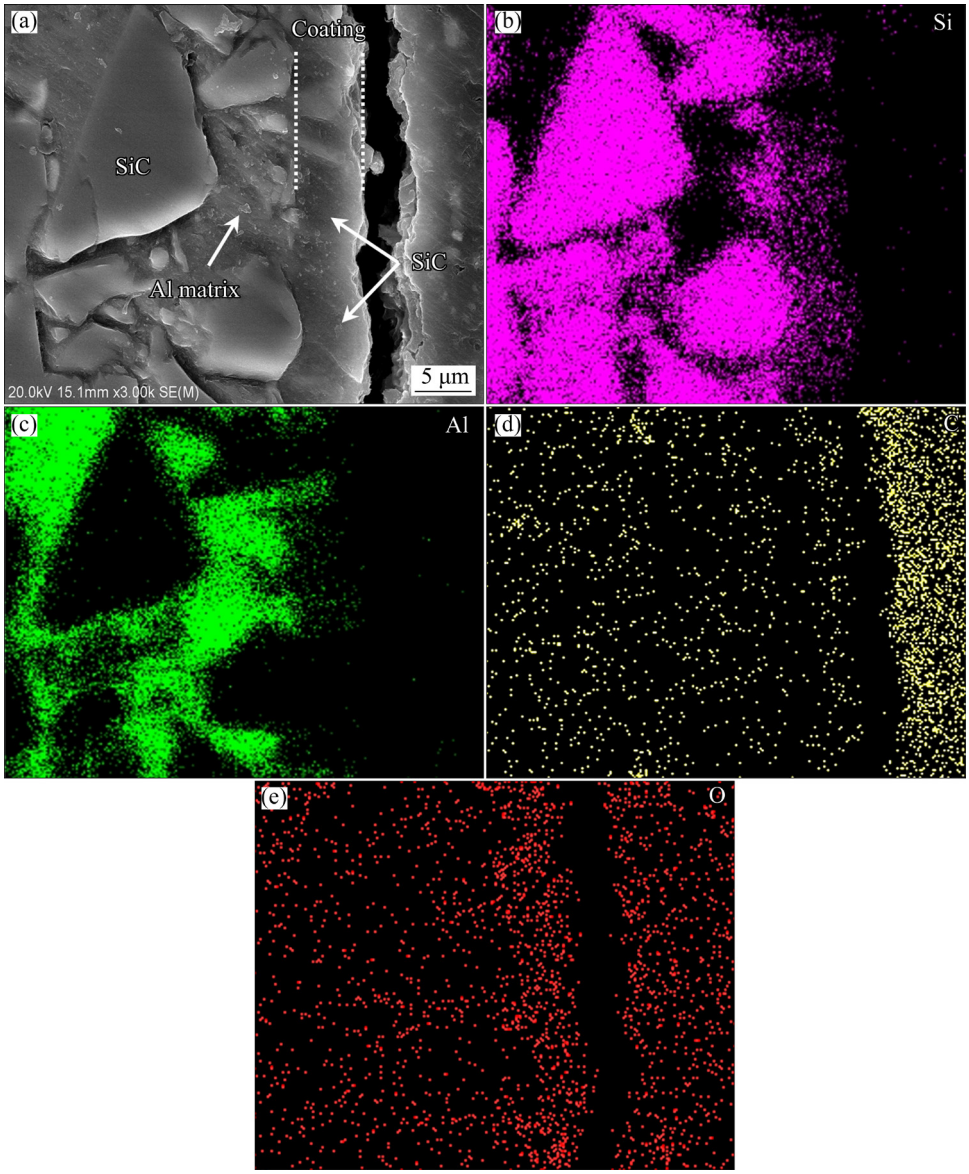

Fig. 9 Cross-sectional microstructure of coating PEO-treated for 1200 s (a) and its elemental mappings (b−e): (a) SEM image; (b) Si; (c) Al; (d) C; (e) O

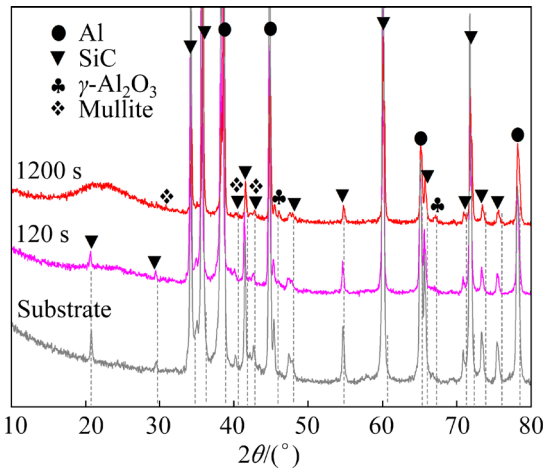

Fig. 10 XRD patterns of PEO-treated Al MMC samples at different oxidation time in silicate solution

than that of γ-Al_2O_3 phase and the high cooling rate of molten oxides in plasma discharge channels for thin PEO coating favors the formation of the γ-Al_2O_3 phase [32]. Furthermore, mullite phase also appears in the PEO coating due to the reaction of Al_2O_3 and SiO_2 phases in plasma discharge channels with the temperature up to 5500 K (see Fig. 5).

The XPS spectra of PEO coating at 120 and 1200 s are shown in Figs. 11 and 12, respectively. As shown in Fig. 11(a), the Al 2p spectrum for the PEO-coated Al MMC at 120 s is deconvoluted into a Gaussian peak with binding energy of 74.42 eV, implying the presence of Al^{3+} corresponding to γ-Al_2O_3 phase [33,34]. The binding energy of Si 2p

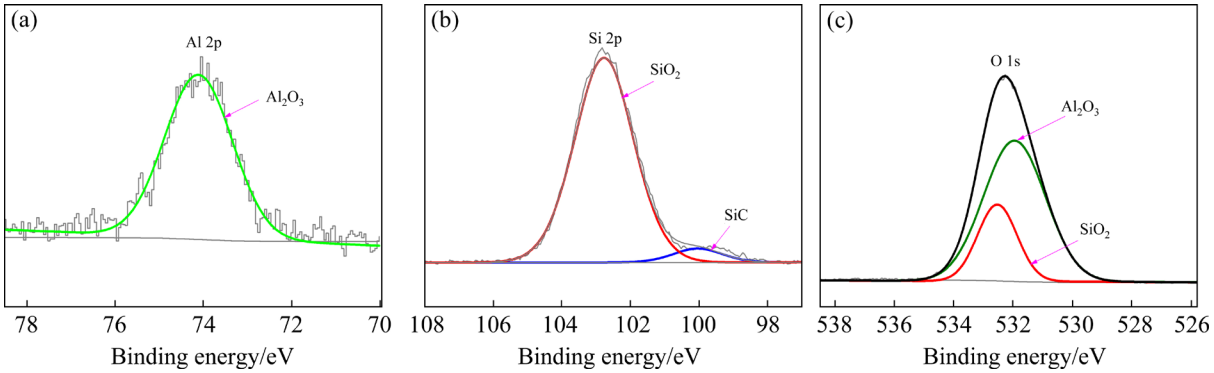

Fig. 11 XPS spectra of PEO coating on 60vol.%SiC_p/Al MMC after 120 s PEO treatment: (a) Al 2p; (b) Si 2p; (c) O 1s

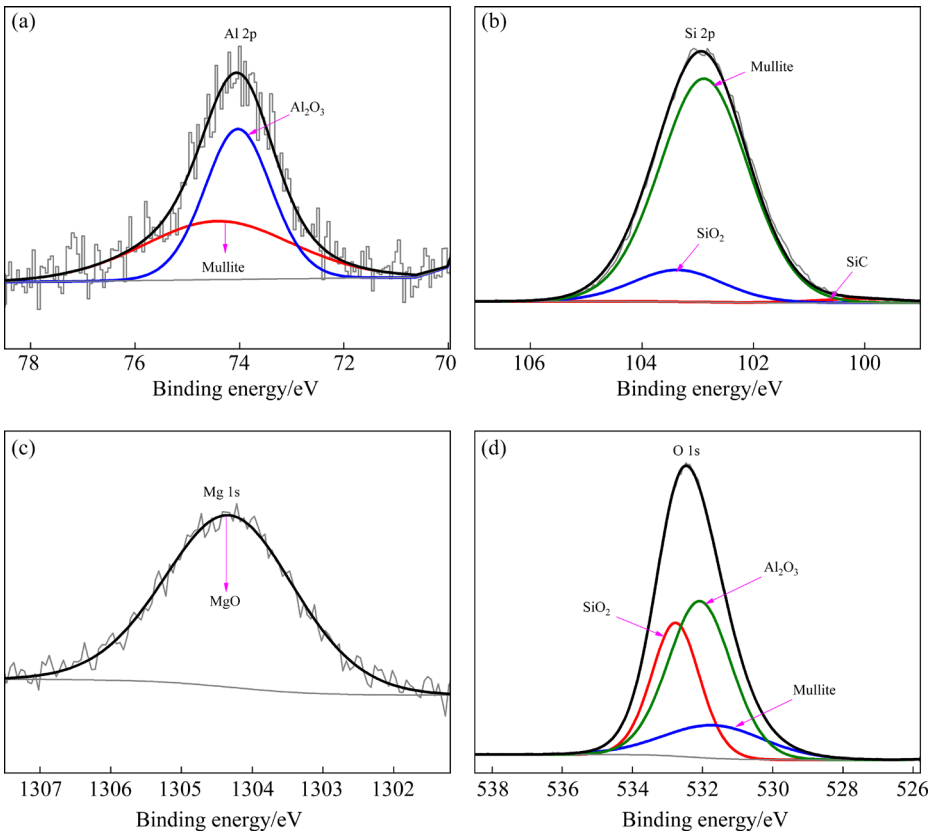

Fig. 12 XPS spectra of PEO coating on 60vol.%SiC_p/Al MMC after 1200 s PEO treatment: (a) Al 2p; (b) Si 2p; (c) Mg 1s; (d) O 1s

spectrum at 103.02 eV in Fig. 11(b) is close to that of SiO_2 [33,35]. Comparing to the XRD pattern of 120 s treatment in Fig. 10, this peak at 103.02 eV should be attributed to the amorphous SiO_2 phase. Moreover, a weak characteristic peak of SiC (100.03 eV) is observed in the spectrum of Si 2p [36], which reveals that a few SiC particles might be remained on the surface of coating after 120 s PEO treatment. In addition, the binding energies of O 1s at 532.00 and 532.74 eV in Fig. 11(c) are attributed to the γ-Al_2O_3 and SiO_2, respectively [37−39].

On the other hand, by comparing Figs. 11 and 12, it is observed that the relatively intensities of Si 2p and O 1s for PEO coating increase by about two orders of magnitude when the oxidation time increases to 1200 s. In the spectrum of Si 2p for the PEO coating at 1200 s, a strong characteristic peak of mullite at 102.70 eV is observed [33], while the characteristic peak of SiC is hardly detected. For SiO_2 in the O 1s spectrum, its relative intensity for coating at 1200 s obviously increases compared with that at 120 s. The Al 2p intensity for coating at 1200 s is also higher than

that at 120 s. These results indicate that more MMC substrate and electrolyte involve in the plasma discharge to form the crystalline phases in the discharge channels with instantaneously high temperature. The Mg 1s spectrum at binding energy of 1304.32 eV is ascribed to the MgO phase, which results from the oxidation of Mg alloying element in the 2009 Al matrix. Hence, the XPS spectra demonstrate that the surface of PEO coating on the Al MMC at 1200 s contains γ-Al_2O_3, SiO_2, mullite and trace MgO. The results are in accordance with XRD patterns in Fig. 10.

3.6 Surface roughness, contact angle and surface free energy of PEO coatings

As displayed in Fig. 13, the surface roughness of PEO coating on 60vol.%SiC_p/Al MMC increases with increasing the oxidation time, and it increases from 0.048 μm of polished Al MMC substrate to 3.404 μm of PEO coating at 1200 s. It is in agreement with the evolution of surface morphologies of PEO coatings in Fig. 6. The roughness of PEO coating at 1200 s is much higher than that of polished Al MMC. This suggests that the plasma discharges form the rough surface on the Al MMC during the PEO process.

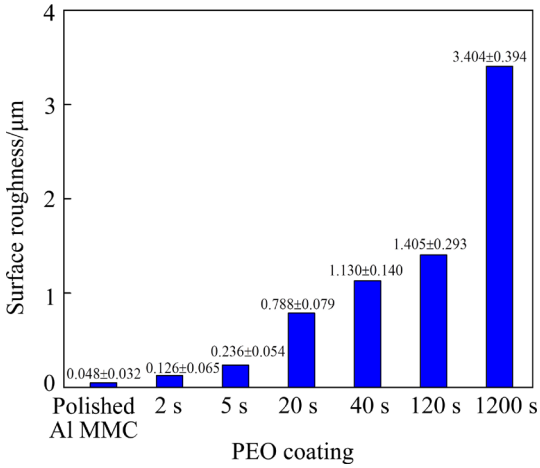

Fig. 13 Surface roughness (R_a) of polished 60vol.%SiC_p/Al MMC and PEO coatings at different oxidation time

It is well known that the water and *n*-hexadecane are common polar liquid and non-polar liquid, respectively [40,41]. The contact angles of water and *n*-hexadecane on the polished 60vol.%SiC_p/Al MMC and the PEO coatings at different oxidation time are shown in Figs. 14(a) and (b), respectively. The contact angle of water on the polished Al MMC surface is 87.47°, which reveals its hydrophilicity. However, the contact angle of water on the PEO coating decreases from 83.93° at 2 s to 72.93° at 40 s, and then increases to 95.86° at 120 s, finally reaches 119.01° at 1200 s. This indicates that the PEO coating is hydrophilic before 40 s and hydrophobic after 120 s.

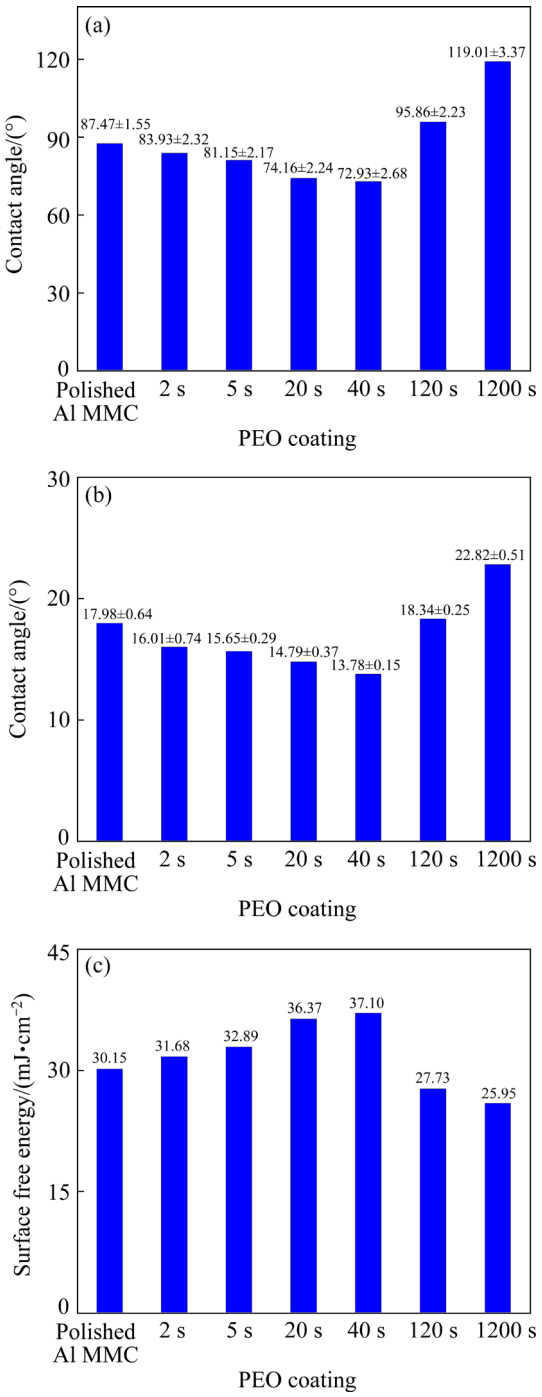

Fig. 14 Contact angles and surface free energy of polished 60vol%SiC_p/Al MMC and PEO coatings at different oxidation time: (a) Water; (b) *n*-hexadecane; (c) Surface free energy

On the other hand, the contact angle of *n*-hexadecane on the polished Al MMC surface is only 13.78° as displayed in Fig. 14(b). Moreover, the evolution of the contact angle of *n*-hexadecane on the PEO coating with oxidation time is similar to that of water on the coating surface. It decreases from 16.01° at 2 s to 13.78° at 40 s, then begins to rise after 120 s, and finally reaches 22.82° at 1200 s. The result suggests that the Al MMC and PEO coatings at different time are oleophilic, whereas the lipophilicity of PEO coating decreases after 120 s.

Furthermore, based on the contact angles of water and *n*-hexadecane in Figs. 14(a) and (b) and their surface tension values in Table 2, the surface free energies of the polished Al MMC and the PEO coatings at different oxidation time are also calculated by Eqs. (2)−(4) [42]:

$$\gamma_L = \gamma_L^d + \gamma_L^p, \quad \gamma_S = \gamma_S^d + \gamma_S^p \tag{2}$$

$$\gamma_L(1+\cos\theta) = 2\sqrt{\gamma_L^d \gamma_S^d} + 2\sqrt{\gamma_L^p \gamma_S^p} \tag{3}$$

$$\gamma_S^d = b^2,\ \gamma_S^p = a^2,$$
$$x = \sqrt{\gamma_L^p/\gamma_L^d},\ y = \gamma_L(1+\cos\theta)/(2\sqrt{\gamma_L^d}) \tag{4}$$

where γ_L and γ_S denote the surface free energies of liquid and solid, respectively. Both of them can be divided into dispersion component (γ_L^d and γ_S^d) and polar component (γ_L^p and γ_S^p). The θ is the contact angle of the liquid on the solid surface. By transforming Eqs. (2) and (3) into the linear regression ($y=ax+b$), the surface free energy of the Al MMC and PEO coatings is obtained.

Table 2 Surface tensions of water and *n*-hexadecane and their components

Liquid	Surface tension/(mN·m^{-1})		
	γ_L	γ_L^d	γ_L^p
Water	72.8	21.8	51.0
n-hexadecane	27.6	27.6	0

As displayed in Fig. 14(c), the surface free energy of polished Al MMC is 30.15 mJ/cm^2, and the surface free energy of the PEO coating increases from 31.68 mJ/cm^2 at 2 s to 37.10 mJ/cm^2 at 40 s, then decreases to 25.95 mJ/cm^2 at 1200 s. The microstructure and chemical constituent of solid surface are two key factors in affecting its wettability [43,44]. In the initial 40 s of PEO process, the SiC particles on the surface of 60vol.%SiC_p/Al MMC is not completely covered by the PEO coating as shown in Figs. 6(a−e). In this stage, the surface feature of SiC particles greatly affects the wettability of the coating surface. Moreover, the hydrophilic groups of SiO_3^{2-} and OH^- in the solution are deposited on the Al MMC surface under the spark discharge, which increases the hydrophilicity of the PEO coating surface. Hence, the PEO coating has relatively low contact angle and high surface free energy before 40 s. After 120 s plasma discharge, the surface of Al MMC is completely covered with a continuous PEO coating (see Figs. 6(f) and (g)). Meanwhile, the mullite ($3Al_2O_3{\cdot}2SiO_2$) and γ-Al_2O_3 phases in the PEO coating affect the electrostatic attraction at the solid/liquid interface, which reduces the surface free energy of the PEO coating and decreases its wettability. Therefore, the PEO coatings have higher contact angle and lower surface free energy after 120 s PEO treatment.

3.7 Electrochemical corrosion

The potentiodynamic polarization curves and EIS plots of bare Al MMC and PEO-coated Al MMC in the 3.5 wt.% NaCl solution are shown in Fig. 15. By fitting the polarization curves in Fig. 15(a), the corrosion potentials (φ_{corr}), corrosion current density (J_{corr}) and polarization resistance (R_p) are determined and listed in Table 3. The φ_{corr} increases from −1.038 V for bare Al MMC to −0.678 V for the PEO-coated Al MMC. The J_{corr} significantly decreases by three orders of magnitude after 1200 s PEO treatment. Meanwhile, the R_p also increases from 3.70×10^2 to 3.69×10^5 Ω·cm^2. These results show that the PEO surface treatment can greatly improve the corrosion resistance of 60vol.%SiC_p/2009 Al MMC.

On the other hand, Fig. 15(b) shows that an inductive loop appears in the Nyquist plot of bare Al MMC. It implies that the pitting corrosion is easy to occur for the bare 60vol.%SiC_p/2009 Al MMC [1,45]. Furthermore, the diameter of capacitive loop for the PEO-coated Al MMC is much larger than that of the bare Al MMC, implying a higher corrosion resistance for the PEO coating. Meanwhile, the disappearance of inductive loop in Nyquist plot of PEO coating indicates that the PEO treatment can suppress the occurrence

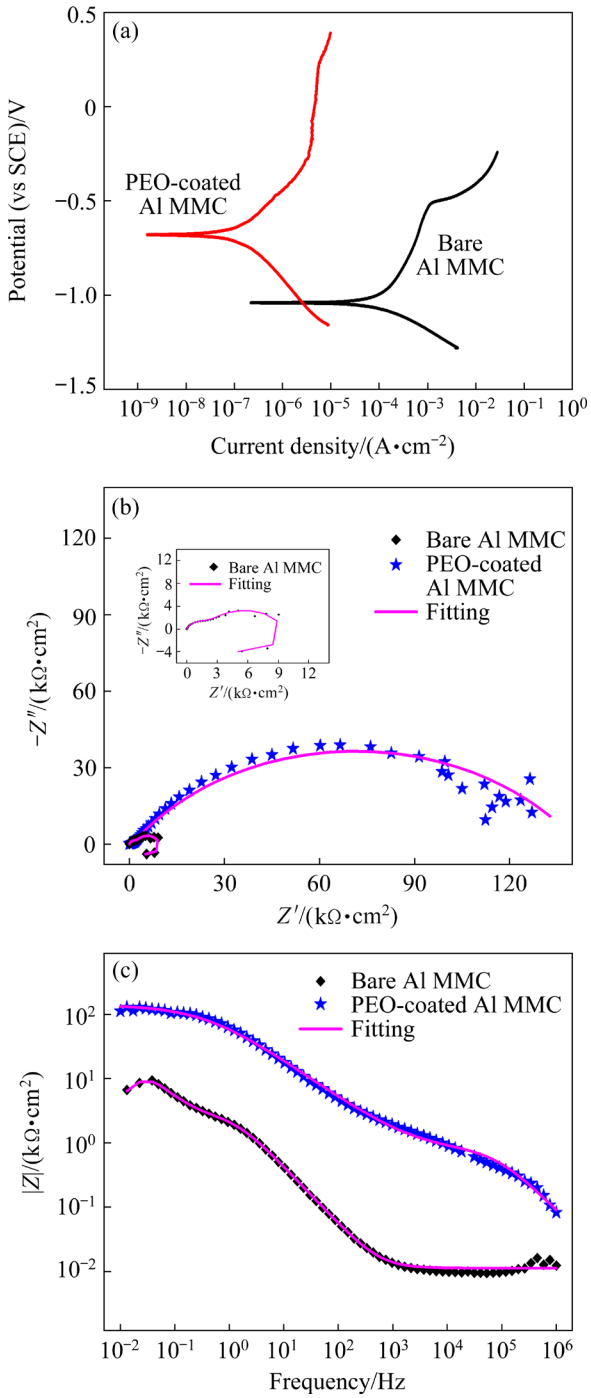

Fig. 15 Electrochemical corrosion tests of bare Al MMC and PEO coating in 3.5 wt.% NaCl solution: (a) Potentiodynamic polarization curves; (b) Nyquist plots; (c) Bode plots

Table 3 Results of potentiodynamic polarization tests of bare Al MMC and PEO-coated Al MMC for 1200 s

Sample	φ_{corr} (vs SCE)/V	J_{corr}/(A·cm^{-2})	R_p/(Ω·cm^2)
Bare Al MMC	−1.038	1.53×10^{-4}	3.70×10^{2}
PEO coating	−0.678	1.98×10^{-7}	3.69×10^{5}

of pitting corrosion on the surface of 60vol.%SiC$_p$/2009 Al MMC. In addition, the Bode plots in Fig. 15(c) displays that the impedance modulus of the PEO-coated Al MMC is one order of magnitude higher than the bare Al MMC in the whole frequency range.

Figure 16 exhibits the equivalent circuits of the EIS plots. R_s is the resistance of the aqueous solution, R_1 is the charge transfer resistance, R_2 is the resistance of the passive film or the PEO coating on the Al MMC, and R_L and L are the inductive resistance and inductance associated with pitting corrosion. Constant phase element (CPE) is defined as $Z=1/[Y_0(j\omega)^n]$, where Y_0 is modulus of admittance, j is the imaginary number, ω is angular frequency, and n is an exponent to characterize the deviation degree of real capacitance from its ideal value ($0<n\leq1$) [1,16].

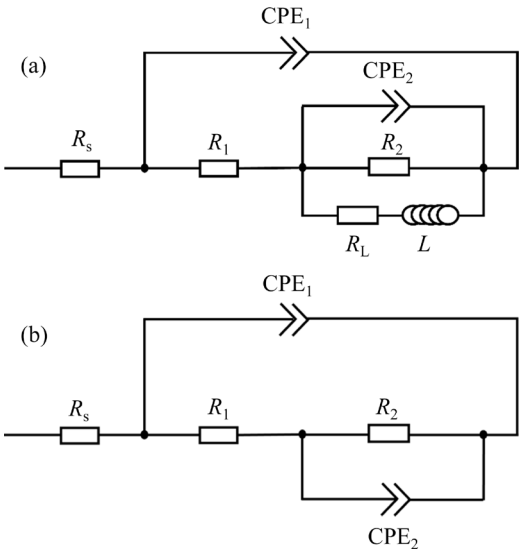

Fig. 16 Equivalent circuits of EIS plots: (a) Bare Al MMC; (b) PEO-coated Al MMC

CPE$_1$ is a constant phase element related to the electric double layer, CPE$_2$ is a constant phase element corresponding to the passive film on bare MMC or the PEO coating on the Al MMC. The corresponding fitting results of EIS plots for bare and PEO-coated Al MMC are listed in Table 4. As shown in Figs. 15(b) and (c), the fitting curves are in good agreement with the experimental data. Moreover, the impedance of the PEO coating is one order of magnitude higher than that of passive film on the Al MMC. It suggests that the PEO treatment can significantly improve the corrosion resistance of the 60vol.%SiC$_P$/2009 Al MMC, which is consistent with the results of polarization tests.

4 Discussion

Based on the above results about the PEO coating growth during the PEO process of 60vol.%SiC_P/2009 Al MMC, a schematic diagram of the PEO coating growth on the Al MMC in silicate solution is displayed in Fig. 17.

When the voltage on the Al MMC anode instantaneously rises to the preset value of 440 V within 1 s (see Fig. 3), a thin alumina barrier layer is simultaneously formed in the Al-rich region on the surface of the Al MMC in terms of Reactions (5) and (6) [46]. However, a SiO_2 barrier layer cannot be formed on the surface of SiC particles owing to their high resistivity. Therefore, the barrier layer only covers the Al matrix rather than the SiC particles as displayed in Fig. 17(a).

$$Al \rightarrow Al^{3+}+3e \quad (5)$$

$$2Al^{3+}+6OH^- \rightarrow Al_2O_3+3H_2O \quad (6)$$

Alkaline substances such as SiO_3^{2-}, PO_4^{3-} and VO_4^{3-} are easily adsorbed on the electrode surface to form gels or insoluble compounds during the PEO process [47,48]. SiO_3^{2-} in the silicate solution will generate OH^- and insoluble compound (SiO_2) by Reactions (7) and (8), respectively [46,49]. As displayed in Fig. 17(a), the insoluble compound (SiO_2) produced by SiO_3^{2-} accumulates on the Al matrix to form a deposition layer under the effect of electric field, and a small amount of the compound is deposited on the surface of SiC particles. Moreover, given the tip or marginal effect of the electrical concentration in the localized region at the SiC/Al interface [27], the compound SiO_2 from silicate solution will be also deposited at the SiC/Al interface.

$$SiO_3^{2-}+2H_2O \rightarrow H_2SiO_3+2OH^- \quad (7)$$

$$2SiO_3^{2-}-4e \rightarrow 2SiO_2+O_2 \quad (8)$$

As shown in Fig. 17(b), spark discharges appear on the Al matrix, while it is difficult for the discharge current on the Al matrix to pass through the SiC particles due to their high resistivity. However, the SiO_3^{2-} absorbed on the electrode surface is

Table 4 Fitting results of EIS plots for bare Al MMC and PEO-coated Al MMC for 1200 s

Sample	R_s/ ($\Omega\cdot cm^2$)	CPE$_1$, Y_0/ ($\Omega^{-1}\cdot cm^{-2}\cdot s^{-n}$)	n_1	R_1/ ($\Omega\cdot cm^2$)	CPE$_2$, Y_0/ ($\Omega^{-1}\cdot cm^{-2}\cdot s^{-n}$)	n_2	R_2/ ($\Omega\cdot cm^2$)	R_L/ ($\Omega\cdot cm^2$)	L/ ($H\cdot cm^2$)
Bare Al MMC	11.2	5.45×10^{-5}	0.91	3110	3.55×10^{-4}	0.88	8.95×10^{3}	2011	9.25×10^{4}
PEO coating	18.3	1.64×10^{-8}	0.86	817	4.05×10^{-6}	0.61	1.41×10^{5}	–	–

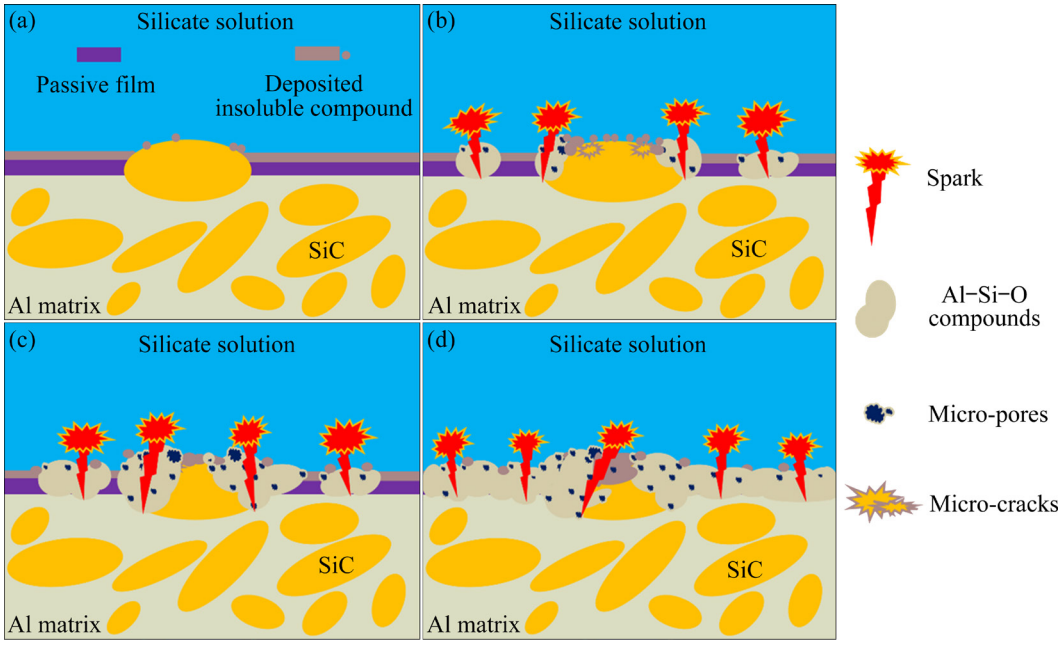

Fig. 17 Schematic diagrams of PEO coating growth on surface of 60vol.%SiC_p/2009 Al MMC

easily to generate the spark discharges [46,48]. Therefore, the absorbed SiO_3^{2-} from silicate solution provides the possibility of spark discharges at the Al/SiC interface, thus the discharge sparks will also appear at the SiC/Al interface. Furthermore, Fig. 8(b) demonstrates that the surface of the PEO coating at 5 s is mainly composed of Si and O elements, and the Al content is rather low. It confirms that more insoluble compounds (SiO_2) from silicate solution gradually deposit on the Al MMC surface under the influence of spark discharge (see Fig. 17(b)). In addition, Figs. 13 and 14 show that in the initial 40 s of plasma discharge, the contact angle of coated Al MMC gradually decreases while its surface roughness and surface free energy gradually increase. It may be ascribed to the deposition of SiO_3^{2-} and OH^- on the coating.

During the PEO treatment on the 60vol.%SiC_P/2009 Al MMC, the average plasma electron temperature is about 5500 K, the Al, SiC, SiO_2 and Al_2O_3 are melted and they react with each other in plasma discharge channels to form Al−Si−O compounds, which mainly consist of mullite phase as shown in Fig. 10. Then, these compounds accumulate at the SiC/Al interface and gradually extend toward the center region of SiC particle surface (see Figs. 6(b) and (c)). Moreover, the micro-pores and micro-cracks in Al−Si−O compounds provide a rapid conduction path for the discharge current through the surface of SiC particles, because these defects create a low electrical resistance region for the conduction of discharge current (see Fig. 17(c)) [4]. Thus, it is possible that the spark discharge extends from the edge of SiC particle to its central region. In addition, as the thickness of PEO coatings on both the Al matrix and SiC/Al interface increases, Fig. 17(d) shows that the discharge positions will extend from the edge of SiC particle to its central area. When the oxidation time reaches 1200 s, a continuous PEO coating of 5.5 μm in thickness is formed on 60vol.%SiC_P/2009 Al MMC as exhibited in Fig. 9(a). At this time, the PEO coating has the largest surface roughness, the highest contact angle and lowest surface free energy (see Figs. 13 and 14). It is believed that the high volume fraction and large size of SiC reinforcement are the main reason for the low growth efficiency of PEO coating. The high fraction SiC particles suppress the ignition of spark discharge and then greatly hinder the rapid growth of PEO coating, which leads to the low efficiency of coating growth. Moreover, the potentiodynamic polarization curves and EIS plots in Fig. 15 reveal that the PEO treatment can significantly enhance the corrosion resistance of the Al MMC. In addition, the SiO_2 results from both the thermal oxidation of SiC particles in plasma discharge channels as described in Ref. [15] and the deposited insoluble compound (Reaction (8)).

5 Conclusions

(1) The spark discharge preferentially occurs in the Al-rich region, then gradually extends from the edge of the SiC particles to their central regions. The deposited SiO_2 on the SiC particle surface plays a key role in the ignition of spark discharge on the surface of SiC particles.

(2) In the regions of Al-rich and SiC/Al interface, the Al, SiC, SiO_2 and Al_2O_3 phases are melted and mixed in high temperature plasma discharge channels up to 5500 K, then Al−Si−O compounds are formed and accumulated in these regions. The micro-pores and micro-cracks in the Al−Si−O compounds provide a rapid path for the discharge current conduction on the surface of SiC particles.

(3) The Al−Si−O compound is mainly composed of mullite ($3Al_2O_3·2SiO_2$) phase.

(4) With the increase of oxidation time, the wettability of PEO coating changes from the hydrophilicity to the hydrophobicity, because the SiC particles and Al matrix are gradually covered by the PEO coating. Meanwhile, the surface free energy of PEO coating reaches a maximum value of 37.10 mJ/cm^2 at 40 s, then decreases to 25.95 mJ/cm^2 at 1200 s.

CRediT authorship contribution statement

Yi-zhao LIAO: Investigations, Formal analysis, Data curation, Writing − Original draft; **Xing-ping WANG:** Data curation, Software, Validation; **Chuan-li GAO:** Data curation; **Qian ZHOU:** Data curation; **Chi XU:** Data curation, Writing − Review & editing; **Xiao-yue JIN:** Visualization; **Jian-cheng DU:** Resources, Software; **Wen-bin XUE:** Supervision, Writing – Review & editing; **Yong-zhong ZHANG:** Materials fabrication.

Declaration of competing interest

The authors declare that they have no known competing financial interests or personal relationships that could have appeared to influence the work reported in this paper.

Data availability

The raw/processed data required to reproduce these findings cannot be shared at this time as the data also forms part of an ongoing study.

Acknowledgments

This research was sponsored by the National Natural Science Foundation of China (Nos. 12105017, 51671032), and Beijing Municipal Natural Science Foundation, China (No. 2172029).

References

[1] KASEEM M, FATIMAH S, NASHRAH N, KO Y G. Recent progress in surface modification of metals coated by plasma electrolytic oxidation: Principle, structure, and performance [J]. Progress in Materials Science, 2021, 117: 100735.

[2] SIMCHEN F, SIEBER M, KOPP A, LAMPKE T. Introduction to plasma electrolytic oxidation—An overview of the process and applications [J]. Coatings, 2020, 10: 628.

[3] YEROKHIN A L, SNIZHKO L O, GUREVINA N L, LEYLAND A, PILKINGTON A, MATTHEWS A. Discharge characterization in plasma electrolytic oxidation of aluminium [J]. Journal of Physics D: Applied Physics, 2003, 36: 2110−2120.

[4] CLYNE T W, TROUGHTON S C. A review of recent work on discharge characteristics during plasma electrolytic oxidation of various metals [J]. International Materials Reviews, 2019, 64: 127−162.

[5] MAHMOUD E R I, ALGAHTANI A, TIRTH V. Study on microstructure characterisation of three different surface coating techniques on 6082-T6 aluminum alloy [J]. Metals and Materials International volume, 2021, 27: 4002−4013.

[6] AN Ling-yun, MA Ying, YAN Xiao-xu, WANG Sheng, WANG Zhan-ying. Effects of electrical parameters and their interactions on plasma electrolytic oxidation coatings on aluminum substrates [J]. Transactions of Nonferrous Metals Society of China, 2020, 30: 883−895.

[7] AGUREEV L, SAVUSHKINA S, ASHMARIN A, BORISOV A, APELFELD A, ANIKIN K, TKACHENKO N, GERASIMOV M, SHCHERBAKOV A, IGNATENKO V, BOGDASHKINA N. Study of plasma electrolytic oxidation coatings on aluminum composites [J]. Metals, 2018, 8: 459.

[8] ZHANG Hong-bin, GENG Ji-wei, LI Xian-feng, CHEN Zhe, WANG Ming-liang, MA Nai-heng, WANG Hao-wei. The micro-arc oxidation (MAO) behaviors of in-situ TiB_2/A201 composite [J]. Applied Surface Science, 2017, 422: 359−371.

[9] CUI Shi-hai, HAN Jian-min, DU Yong-ping, LI Wei-jing. Corrosion resistance and wear resistance of plasma electrolytic oxidation coatings on metal matrix composites [J]. Surface and Coatings Technology, 2007, 201: 5306−5309.

[10] ERARSLAN Y. Wear performance of in-situ aluminum matrix composite after micro-arc oxidation [J]. Transactions of Nonferrous Metals Society of China, 2013, 23: 347−352.

[11] ARUNKUMAR S, SUNDARAM M S, KANNA K S, VIGNESHWARA S. A review on aluminium matrix composite with various reinforcement particles and their behaviour [J]. Materials Today: Proceedings, 2020, 33: 484−490.

[12] MOHANAVEL V, RAJAN K, KUMAR S S, UDISHKUMAR S, JAYASEKAR C. Effect of silicon carbide reinforcement on mechanical and physical properties of aluminum matrix composites [J]. Materials Today: Proceedings, 2018, 5: 2938−2944.

[13] WANG Y Q, WANG X J, GONG W X, WU K, WANG F H. Effect of SiC particles on microarc oxidation process of magnesium matrix composites [J]. Applied Surface Science, 2013, 283: 906−913.

[14] XUE Wen-bin. Features of film growth during plasma anodizing of Al 2024/SiC metal matrix composite [J]. Applied Surface Science, 2006, 252: 6195−6200.

[15] LIU Run, WENG Ning, XUE Wen-bin, HUA Ming, LIU Guan-jun, LI Wen-fang. Analyses of reinforcement phases during plasma electrolytic oxidation on magnesium matrix composites [J]. Surface and Coatings Technology, 2015, 269: 212−219.

[16] DU Chun-yan, HUANG Shu-tao, YU Xiao-lin, WANG Quan-zhao, ZHAO Hui. Microstructure and properties of plasma electrolytic oxidation coating on 55%SiC_p/Al matrix composites [J]. Surface and Coatings Technology, 2021, 420: 127321.

[17] HONG Yu, WANG Wu-jie, LIU Jia-qin, TANG Wen-ming, WU Yu-cheng. Effect of porosity and interface structures on thermal and mechanical properties of SiC_p/6061 Al composites with high volume fraction of SiC [J]. Transactions of Nonferrous Metals Society of China, 2019, 29: 941−949.

[18] TENG Fei, YU Kun, LUO Jie, FANG Hong-jie, SHI Chun-li, DAI Yi-long, XIONG Han-qing. Microstructures and properties of Al−50%SiC composites for electronic packaging applications [J]. Transactions of Nonferrous Metals Society of China, 2016, 26: 2647−2652.

[19] LIU Run, WU Jie, XUE Wen-bin, QU Yao, YANG Chao-lin, WANG Bin, WU Xian-ying. Discharge behaviors during plasma electrolytic oxidation on aluminum alloy [J]. Materials Chemistry and Physics, 2014, 148: 284−292.

[20] HUSSEIN R O, NIE X, NORTHWOOD D O, YEROKHIN A L, MATTHEWS A. Spectroscopic study of electrolytic plasma and discharging behaviour during the plasma electrolytic oxidation (PEO) process [J]. Journal of Physics D: Applied Physics, 2010, 43: 105203.

[21] WEI Kei-jian, ZHANG Yi-fan, YU Jia-hao, LIU Rui-hong, DU Jian-cheng, JIANG Fu-bing, XUE Wen-bin. Analyses of hydrogen release on zirlo alloy anode during plasma electrolytic oxidation [J]. Materials Chemistry and Physics, 2020, 251: 123054.

[22] YANG Xuan, CHEN Lin, QU Yao, LIU Run, WEI Kei-jian, XUE Wen-bin. Optical emission spectroscopy of plasma electrolytic oxidation process on 7075 aluminum alloy [J]. Surface and Coatings Technology, 2017, 324: 18−25.

[23] LEE H Y, TSUI F C, LEE Y C. Structural and microstructural studies on SiC−SiO_2 ceramic composites [J]. Materials Chemistry and Physics, 2019, 233: 203−212.

[24] KVANDE H, DRABLØS P A. The aluminum smelting process and innovative alternative technologies [J]. Journal of Occupational and Environmental Medicine, 2014, 56(5 Suppl): s23−s32.

[25] ZHU Bai-wei, FEDEL M, ANDERSSON N E, LEISNER P, DEFLORIAN F, ZANELLA C. Effect of Si content and morphology on corrosion resistance of anodized cast Al−Si alloys [J]. Journal of the Electrochemical Society, 2017, 164: C435−C441.

[26] LI Kang, LI Wen-fang, ZHANG Guo-ge, ZHU Wen, ZHENG Feng-hua, ZHANG Dong-qiao, WANG Min. Effects of Si phase refinement on the plasma electrolytic oxidation of eutectic Al−Si alloy [J]. Journal of Alloys and Compounds, 2019, 790: 650−656.

[27] WANG Lin-lin, NIE X. Silicon effects on formation of EPO oxide coatings on aluminum alloys [J]. Thin Solid Films, 2006, 494: 211−218.

[28] WANG Xing-ping, WEI Kei-jian, GUAN Hao-hao, XU Chi, XUE Wen-bin, ZHANG Yan-wei, WANG Rong-shan. High temperature oxidation of Zr−1Nb alloy with plasma electrolytic oxidation coating in 900−1200 °C steam environment [J]. Surface and Coatings Technology, 2021, 407: 126768.

[29] WANG Xing-ping, GUAN Hao-hao, LIAO Yi-zhao, ZHU Ming-hao, XU Chi, JIN Xiao-yue, LIAO Bin, XUE Wen-bin, ZHANG Yan-wei, BAI Guang-hai, WANG Rong-shan. Enhancement of high temperature steam oxidation resistance of Zr−1Nb alloy with ZrO_2/Cr bilayer coating [J]. Corrosion Science, 2021, 187: 109494.

[30] XUE Wen-bin, SHI Xiu-ling, HUA Ming, LI Yong-liang. Preparation of anti-corrosion films by microarc oxidation on an Al−Si alloy [J]. Applied Surface Science, 2007, 253: 6118−6124.

[31] KALKANC1 H, KURNAZ S C. The effect of process parameters on mullite-based plasma electrolytic oxide coatings [J]. Surface and Coatings Technology, 2008, 203: 15−22.

[32] XUE Wen-bin, DENG Zhi-wei, LAI Yon-chun, CHEN Ru-yi. Analysis of phase distribution for ceramic coatings formed by microarc oxidation on aluminum alloy [J]. Journal of the American Ceramic Society, 1998, 81: 1365−1368.

[33] AYAME A, KITAGAWA T. X-ray photoelectron spectroscopic measurement and chemical characteristics of silica, alumina and silica-alumina [J]. Bunseki Kagaku, 1991, 40: 673−678.

[34] OKAMOTO Y, ADACHI T, MAEZAWA A, IMANAKA T. Effect of ZnO addition on cobalt–alumina interaction species [J]. Bulletin of the Chemical Society of Japan, 1991, 64: 236−242.

[35] FINSTER J. SiO_2 in 6:3 (stishovite) and 4:2 Co-ordination—characterization by core level spectroscopy (XPS/XAES) [J]. Surface and Interface Analysis, 1988, 12: 309−314.

[36] DIDZIULIS S V, FLEISCHAUER P D. Effects of chemical treatments on SiC surface composition and subsequent MoS_2 film growth [J]. Langmuir, 1990, 6: 621−627.

[37] WAGNER C D, PASSOJA D E, HILLERY H F, KINISKY T G, SIX H A, JANSEN W T, TAYLOR J A. Auger and photoelectron line energy relationships in aluminum–oxygen and silicon–oxygen compounds [J]. Journal of Vacuum Science and Technology, 1982, 21: 933−944.

[38] DUA A K, GEORGE V C, AGARWALA R P. Characterization and microhardness measurement of electron-beam-evaporated alumina coatings [J]. Thin Solid Films, 1988, 165: 163−172.

[39] ANDERSON P R, SWARTZ W E. X-ray photoelectron spectroscopy of some aluminosilicates [J]. Inorganic Chemistry, 1974, 13: 2293−2294.

[40] YOU Peng, LV Xin-lian, WU Hai-peng. Surface free energy of coated paper measured by Owens method [J]. Journal of Shaanxi University of Science & Technology (Natural Science Edition), 2011, 29: 36−39. (in Chinese)

[41] DAVID J G, JOEY W S, CHRISTOPHER J C, DONALD G T. General semiempirical quantum mechanical solvation model for nonpolar solvation free energies. n-hexadecane [J]. Journal of the American Chemical Society, 1995, 117: 1057−1068.

[42] RBIHI S, ABOULOUARD A, LAALLAM L, JOUAITI A. Contact angle measurements of cellulose based thin film composites: wettability, surface free energy and surface hardness [J]. Surfaces and Interfaces, 2020, 21: 100708.

[43] DAS A, CHAWLA V, MATOS R S, FILHO H D F, YADAV R P, TĂLU Ş, KUMAR S. Surface microtexture and wettability analysis of quasi two-dimensional (Ti, Al) N thin films using fractal geometry [J]. Surface and Coatings Technology, 2021, 421: 127420.

[44] MONTEIRO E S, SOARES F M S, NUNES L F, SANTANA A I C, BIASI R S, ELIAS C N. Comparison of the wettability and corrosion resistance of two biomedical Ti alloys free of toxic elements with those of the commercial ASTM F136 (Ti−6Al−4V) alloy [J]. Journal of Materials Research and Technology, 2020, 9: 16329−16338.

[45] WEI Bing-jian, CHENG Yu-lin, LIU Yuan-yuan, ZHU Zhun-da, CHENG Ying-liang. Corrosion and wear resistance of AZ31 Mg alloy treated by duplex process of magnetron sputtering and plasma electrolytic oxidation [J]. Transactions of Nonferrous Metals Society of China, 2021, 31: 2287−2306.

[46] WANG Shuai-xing, LIU Xiao-hui, YIN Xiao-le, DU Nan. Influence of electrolyte components on the microstructure and growth mechanism of plasma electrolytic oxidation coatings on 1060 aluminum alloy [J]. Surface and Coatings Technology, 2020, 381: 125214.

[47] STOJADINOVIC S, VASILIC R, BELCA I, PETKOVIC M, KASALICA B, NEDIC Z, ZEKOVIC L. Characterization of the plasma electrolytic oxidation of aluminium in sodium tungstate [J]. Corrosion Science, 2010, 52: 3258−3265.

[48] SNIZHKO L O, YEROKHIN A L, PILKINGTON A, GUREVINA N L, MISNYANKIN D O, LEYLAND A, MATTHEWS A. Anodic processes in plasma electrolytic oxidation of aluminium in alkaline solutions [J]. Electrochimica Acta, 2004, 49: 2085−2095.

[49] GU Wei-chao, LV Guo-hua, CHEN Huan, CHEN Guang-liang, FENG Wen-ran, ZHANG Gu-ling, YANG Si-ze. Investigation of morphology and composition of plasma electrolytic oxidation coatings in systems of Na_2SiO_3−NaOH and $(NaPO_3)_6$−NaOH [J]. Journal of Materials Processing Technology, 2007, 182: 28−33.

60%SiC_p/2009 铝基复合材料表面等离子体电解氧化膜的生长和表征

廖燚钊[1,2]，王兴平[1,2]，高川力[1,2]，周 茜[1,2]，徐 驰[1,2]，金小越[2]，杜建成[1,2]，薛文斌[1,2]，张永忠[3]

1. 北京师范大学 核科学与技术学院 射线束技术教育部重点实验室，北京 100875；
2. 北京市科学技术研究院 辐射技术研究所，北京 100875；
3. 中国有研科技集团有限公司，北京 100088

摘 要：在硅酸盐溶液中采用等离子体电解氧化技术在 60%SiC_P(体积分数)/2009 铝基复合材料表面制备陶瓷膜。研究氧化膜的显微组织、成分、润湿性及其耐腐蚀性能，探讨 SiC 颗粒表面火花放电的产生机理。结果表明，来自硅酸盐溶液的不溶性化合物(SiO_2)使 SiC 颗粒表面产生火花放电，Al−Si−O 化合物中的缺陷为 SiC 颗粒表面放电电流的传导提供优先路径。1200 s 时铝基复合材料表面形成 5.5 μm 厚的均匀膜层，膜层的表面自由能在 40 s 时达到最大值 37.10 mJ/cm^2，并在 1200 s 时下降到 25.95 mJ/cm^2。此外，等离子体电解氧化处理可以显著提高复合材料的耐蚀性。

关键词：等离子体电解氧化；铝基复合材料；SiC 增强颗粒；火花放电；润湿性；耐蚀性

(Edited by Xiang-qun LI)